JOURNAL OF MECHANICS OF CONTINUA AND MATHEMATICAL SCIENCES
www.journalimcms.org

ISSN (Online) : 2454 -7190 Vol.-21, No.-07, July (2026) pp 130-145 ISSN (Print) 0973-8975

DESIGN AND ANALYSIS OF AN ASYMMETRIC KITE-SHAPED PATCH ANTENNA FOR 5G/6G UAV APPLICATIONS

Tamara Z. Fadhil[1], Ameer A. Kareim Al-Sahlawi[2]

[1]Department of Mobile Communications and Computing Engineering, College of Engineering, University of Information Technology and Communications (UOITC), Baghdad 10013, Iraq.

[2]Department of Electrical Engineering, Faculty of Engineering, University of Kufa, Kufa, Najaf Governorate, Iraq.

Email: [1]tamara.zuhair@uoitc.edu.iq, [2]ameera.abbas@uokufa.edu.iq

Corresponding Author: **Tamara Z. Fadhil**

https://doi.org/10.26782/jmcms.2026.07.00008

(Received: April 18, 2026; Revised: June 28, 2026; Accepted: July 12, 2026)

Abstract

A high-gain, beam-tilted, kite-shaped patch antenna design is proposed for millimeter-wave (mmWave) communication and autonomous sensing in unmanned aerial vehicles (UAVs). The proposed antenna is based on a novel asymmetric kite-shaped radiator and a non-uniform via fence to achieve passive beam steering without the complications of phased-array architectures. Full-wave simulations performed in CST Studio Suite show that the impedance bandwidth is −10 dB at the center frequency of 30 GHz in the Ka band (26–38 GHz). The antenna achieves a peak realized gain of 8.58 dBi, with a passive beam tilt of 49° and an 80.2° 3 dB beamwidth, and is designed for drone-to-ground (D2G) wireless communication applications and lateral obstacle detection. The antenna is integrated on a UAV platform for practical testing. The results indicate that a 5 mm air gap is effective in suppressing platform-induced electromagnetic coupling, with minimal beam and pattern distortion. The proposed structure is a compact, lightweight, single-port design that offers a low-complexity solution for next-generation 5G/6G UAV communication systems without requiring a phased array or mechanical beam-steering mechanism.

Keywords: Kite-shaped antenna, mmWave, beam tilting, UAV collision avoidance, 5G/6G, high-gain patch antenna.

I. Introduction

Significant changes are being observed in modern wireless communication systems due to the rapid advancement of unmanned aerial vehicles and autonomous transportation systems [XXVI], [V]. According to the literature, migration to millimeter-wave frequency bands, i.e., the Ka band (26.5–40 GHz), is not only important but also inevitable for meeting the high data-rate requirements of 5G and 6G networks [XXXV], [II]. However, as we operate at 30 GHz, we face significant electromagnetic challenges, including high path loss, oxygen absorption, and pronounced shadowing effects [XXXI], [I]. To maintain a strong link as the UAVs tilt and change direction, the drone-based antennas must provide high realized gain, high efficiency, and, more importantly, high directional accuracy [IV], [XXXVII].

Although the microstrip patch antenna is popular for its compact profile, lightweight, and easy integration with the aerodynamics of the drone [XXVII], [XXXII], it has the disadvantage of radiating a broadside field that does not change direction in response to the drone's tilting motion [XXIII]. In the field of drone-based autonomous sensing, the main problem is the "lateral awareness" problem. The microstrip patch antenna, which radiates its field perpendicular to the patch, does not have its main beam radiate in the direction required for collision avoidance, side-scanning radar, and drone-ground communication [XXXIV], [XXV]. The traditional off-axis radiation techniques, e.g., mechanical gimbal stabilization, increase weight and mechanical complexity, thereby compromising flight time [XIX]. Electronic beam steering with phased arrays is also effective but requires complex feeding networks, expensive phase shifters, and sophisticated control mechanisms [XXVI], [XV]. As a result, there is increasing interest in "static" antenna solutions that tilt the beam by structural or geometrical modifications [XXXIII], [XXIV]. This paper proposes a novel "static" antenna solution that has the advantages of robustness, cost-effectiveness, and maintenance-free operation.

The choice of the dielectric substrate is vital to the design of high-efficiency mmWave antennas. Dielectric losses and surface waves can be problematic at 30 GHz [XX]. This work employs the Rogers RT5880 substrate. This substrate has a low dielectric constant of $\varepsilon r = 2.2$. Moreover, it has an exceptionally low loss tangent of 0.0009 at 10 GHz [III], [XXIX]. Low εr allows more of the electric field to pass through the air, allowing the fringing fields to be high and thus providing a high radiation capability for the antenna [XII]. The thickness of the substrate is optimized at 0.787 mm, which can simultaneously achieve the maximum impedance bandwidth and suppress the unwanted surface wave that could affect the far-field pattern. Furthermore, the multi-layered structure of the proposed antenna incorporates a kite-shaped radiating patch on the top layer and a strategic parasitic layer, which further focuses the electromagnetic energy and increases the peak realized gain [XXIII], [XXXVI].

Building on the concept of structural modification, recent research has explored various techniques to manipulate radiation characteristics without relying on active components. For example, capacitive via-fence loading techniques have been proposed to increase the beamwidth of microstrip antennas by providing a vertical current distribution via metalized vias, thereby enabling coverage in both the E and H planes [XXXIV], [XXXV]. Cavity-backed structures and substrate-integrated coaxial lines (SICL) have also been used to achieve high-gain, stable radiation characteristics with low back-lobe levels for applications in the millimeter-wave (mmWave) band [XXV], [IV]. Although these designs show promising results, they often focus on providing broadside radiation and conical beams for omnidirectional coverage [XIX], [XIII]. For example, a conical beam provides a 360-degree field of view but may sacrifice directivity in directions off the axis. In long-range lateral sensing and point-to-point communication at 30 GHz, a highly directive beam with a large tilt angle is required to ensure a robust signal-to-noise ratio (SNR) and prevent interference from undesired directions [XXVI], [XXI].

The current paper bridges this research gap by proposing a new Kite-shaped Patch Antenna that leverages structural asymmetry and non-uniform via-fence loading to maximize beam tilting. The proposed structure inherently breaks the symmetry of the surface current distribution of the radiating element. In combination with the 6:4 via ratio on the lateral edges of the radiator, this results in a phase perturbation across the antenna aperture. As a result, the Poynting vector is deflected significantly from the zenith direction, resulting in a main beam direction of 49.0° at 30 GHz. In addition, the proposed design achieves a maximum realized gain of 8.3 dBi, enabling high-performance transmission for drone communication. In contrast to existing solutions that require the implementation of complex multilayer apertures [XXXIII] or active beam steering mechanisms [XXVI], [XV], the proposed Kite-shaped Patch Antenna is a single-element solution that is easy to integrate into the aerodynamic structures of modern Unmanned Aerial Vehicles (UAVs). Table 3 provides a detailed comparison of the proposed antenna with state-of-the-art tilted-beam antenna designs.

II. Design Methodology

The design approach for the proposed Kite-shaped antenna is segmented into four developmental phases to attain a stable 49.0° beam squint and a realized gain of 8.3 dBi at 30 GHz.

Evolution of the Design

The suggested antenna was developed in four independent phases (Cases 1–4) to examine the interplay of geometric asymmetry, reactive loading, and multilayer coupling.

1) Case 1: Conventional Rectangular Patch Antenna (Benchmark)

The design starts with a conventional rectangular microstrip patch antenna designed to resonate at 30 GHz on a Rogers RT5880 substrate, as shown in Fig.1. In the standard arrangement of the rectangular microstrip antenna, the current density is distributed over the length of the antenna. Consequently, the radiation pattern is oriented at an angle of θ = 0° toward the boresight.

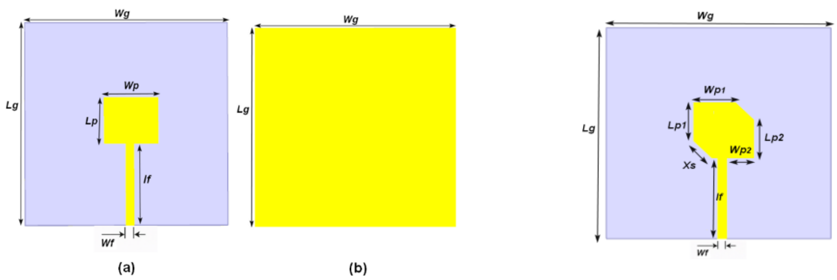

Fig.1. (a) Symmetric Microstrip Patch Benchmark. Fig.2 Asymmetric Conversion Kite Patch. (b) Bottom View: Common Solid Ground Plane.

2) *Case 2: Kite-Shaped Radiator (Geometric Asymmetry)*

To create beam squint, a conventional rectangular patch was modified to a Kite-shaped radiator. The patch's transverse dimensions were set to Wp_1 = 4.0 mm and Wp_2 = 2.8 mm. This created a geometric asymmetry that introduced a phase perturbation due to non-uniform current path lengths, as shown in Fig.2. This effectively created beam squint by steering the main beam away from the zenith direction. The following (1)–(3) adhere to the transmission-line microstrip antenna formulation provided in [XXX].

Guided phase constant:

$$\beta = k_0\sqrt{\varepsilon_{\text{eff}}} \tag{1}$$

Aperture phase difference:

$$\Delta\phi = \beta\ \Delta l \tag{2}$$

Free-space wavenumber:

$$k_0 = \frac{2\pi}{\lambda_0} \tag{3}$$

3) *Case 3: Non-Uniform Via-Fence Loading (Modal Control)*

In the third step, two arrays of metallized via were embedded in the substrate. While the initially symmetric via configuration was considered to achieve better improvement of the isolation, the non-uniform via fence 4:6 configuration was adopted as shown in Fig.3. This configuration acts as a reactive loading network to moderate substrate modes and surface waves. While efforts were made to exploit the via to re-center the beam, the phase gradient of the Kite geometry was found to dominate, thus preserving the beam tilt of 49.0°. Nevertheless, the via greatly improved the front-to-back ratio and radiation stability. The following (4),(5) equations follow the equivalent LC surface model described in [XXVIII],[XIV]

Equivalent surface impedance:

$$Z_s = j\left(\omega L_{\text{via}} - \frac{1}{\omega C_{\text{gap}}}\right) \tag{4}$$

Resonant condition:

$$\omega_0 = \frac{1}{\sqrt{L_{\text{via}} C_{\text{gap}}}} \tag{5}$$

4) *Case 4: Multilayer Parasitic Configuration (Final Proposed Design)*

In the last step of the optimization process, the parasitic director patch was suspended above the driven Kite radiator, as shown in Fig. 4, by two layers of Rohacell 51 IG foam material (Ha_1 = 0.9 mm, Ha_2 = 0.6 mm). Due to the ultra-low permittivity of the spacer material (ε_r = 1.05), strong near-field electromagnetic coupling is observed between the driven and parasitic patches, as shown in Fig.4. This coupling reduces the beamwidth and increases the directivity, thus increasing the realized gain to 8.3 dBi while preserving the beam tilt of 49.0°.

Coupling coefficient:

$$k = \frac{W_{12}}{\sqrt{W_1 W_2}} \tag{6}$$

Mutual stored energy:

$$W_{12} = \frac{1}{2}\int_V (\varepsilon E_1 \cdot E_2 + \mu H_1 \cdot H_2) dV \quad (7)$$

(6), (7) equations follow the reaction theorem formulation in [VI], [XVII].

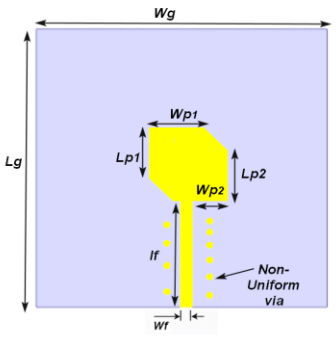

Fig.3. Non-Uniform Via-Fence Configuration.

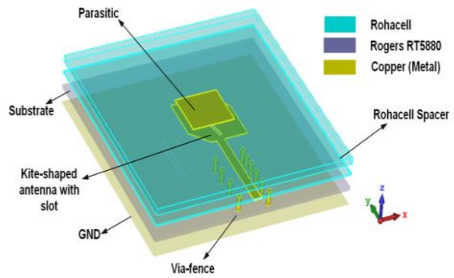

Fig.4. The proposed multilayer antenna configuration in an exploded view.

III. Analysis of Design Evolution and Impedance Matching

A conventional square patch (Case 1) was used to start the layout development process since it allowed for a baseline resonance without the phase manipulation required for high-angle steering. The development of a kite-shaped radiator with a diagonal reactive slot (Case 2) prevented surface current drift and achieved the phase gradient required for steering. The introduction of a non-uniform via fence (Case 3) notably progressed impedance matching, as evidenced through a discount in the mirrored image underneath -20 dB as shown in Fig.5. The non-uniform via fence acted as a modal management device, doing away with undesirable surface waves that regularly accompany asymmetric systems. The final step concerned the integration of a parasitic director and Rohacell 51 spacers (Case 4), which facilitated close-to-field electromagnetic couplings. The multilayer integration substantially stepped forward impedance matching, achieving a deep resonance at -64 dB around 31.5 GHz at the same time as keeping a regular beam squint at 49° for high-gain applications.

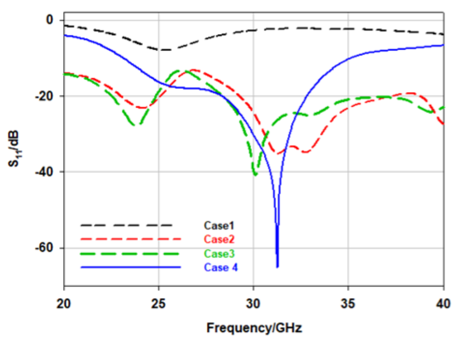

Fig.5. Simulated Reflection Coefficients S_{11} Across the Four Design Cases

IV. Parametric Study and Optimization

Two primary structural parameters were systematically investigated to achieve the desired 49.0° beam squint. At the same time, make sure optimal impedance matching: (i) the diagonal reactive slot's geometry and (ii) the vertical space between the driven element and the parasitic director.

i. The Diagonal Reactive Slot's Effect

A thorough parametric analysis of the diagonal reactive slot was conducted to achieve ideal beam steering and impedance matching. Because they regulate the reactive loading on the kite-shaped radiator, the proportions of this slot are crucial.

The half-wavelength slot model can be used to estimate the effect of the diagonal reactive slot on the resonance characteristics. One way to express the fundamental slot resonance frequency is as [XXX],[VI],[XVII]:

$$f_{\text{slot}} \approx \frac{c}{2L_{\text{slot}}\sqrt{\frac{\varepsilon_r+1}{2}}} \tag{8}$$

L_{slot} is the primary factor that controls frequency tuning. This relationship allows for an approximation of the first-order frequency sensitivity as

$$\frac{\partial f_0}{\partial L_{\text{slot}}} \approx -\frac{f_0}{L_{\text{slot}}} \tag{9}$$

This demonstrates that the resonance moves toward lower frequencies as the slot length increases. Along with frequency control, the slot width w modifies the reactive loading and coupling strength along the perturbed current channel, which affects the impedance matching depth. The variance in matching level near the ideal configuration can be phenomenologically described as [VI]:

$$\Delta|S_{11}|_{\text{dB}} \approx \left(\frac{\partial|S_{11}|_{\text{dB}}}{\partial W_{\text{slot}}}\right)\Delta W_{\text{slot}} \tag{10}$$

Implying that slight slot width decreases improve the resonance null's sharpness. Additionally, the induced aperture phase gradient is directly influenced by the slot angle θslot. The slot-induced phase perturbation scales as follows when approximating at small angles:

$$\Delta\phi_{\text{slot}} \propto k_0\sqrt{\varepsilon_{\text{eff}}}L_{\text{slot}}\sin(\theta_{\text{slot}}) \tag{11}$$

The slot angle (*SlotA*), length (*SlotL*), offset (*Slot OffsetX*, and width (*Slot W*) of ten distinct iterations (3D Run IDs) were examined in a slot geometric iteration analysis. The reflection coefficient (S_{11}) data was used to assess each iteration's performance. Table 1 provides a summary of the particular values for every run.

Table 1. Parametric variations of the diagonal slot geometry

3D Run ID	SlotA	SlotL	SlotOffsetX	SlotW
1	45	2.6	0.15	0.3
2	15	2.6	0.4	0.3
3	15	2.6	0.5	0.3

4	10	3	0.7	0.4
5	50	3	0.1	0.2
6	5	3	0.1	0.2
7	0	2	0.1	0.2
8	20	2	0.1	0.2
9	15	1.5	0.1	0.2
10	15	3	0.1	0.2

The optimized slot configuration provides a significant resonance null at −65 dB at 31.5 GHz, which is a very good impedance match with the 50 Ω feed line. The results show that the diagonal slot not only controls the phase distribution but also significantly enhances return-loss performance. The findings in Fig.6 show that the slot dimensions have a considerable impact on the resonance frequency and matching depth.

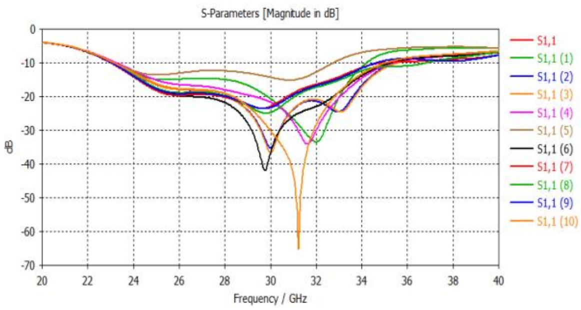

Fig. 6 illustrates the simulated S_{11} for systematic variations of the slot geometry.

Measurable alterations in the resonance position around 30–31.5 GHz are caused by changes in the reactive contribution caused by variations in slot length and orientation. Excellent impedance matching to the 50 Ω feed line is proven by a prominent resonance null that processes −65 dB at 31.5 GHz, which is produced by an optimized slot arrangement. The findings display that the diagonal slot greatly improves go-back loss overall performance, similarly to controlling the section distribution.

ii. Impact of Parasitic gap Height (z_{par})

In order to adjust the near-field interaction between the driven kite-shaped radiator and the parasitic director, the distance z_{par} between the layers was varied. This spacer element controls the strength of interaction between electromagnetic fields, thus affecting its impedance characteristics and radiation efficiency.

Consequently, the beam guiding system is established. The near-field coupling strength is mostly controlled by the vertical distance, represented by Z_{par}, between the driven radiator and the parasitic director. An evanescent-field decay model could be used to represent this interaction [XXX], [VII] :

$$k\left(z_{\text{par}}\right) \approx k_0 e^{-\alpha |z_{\text{par}}|} \tag{12}$$

where the vertical decay constant is denoted by α. Stronger power transfer to the parasitic element results from the coupling coefficient increasing exponentially with decreasing spacing. The coupling-modified input impedance and the accompanying reflection coefficient can be connected as

$$|S_{11}| \approx \left|\frac{Z_{\text{in}}(k)-Z_0}{Z_{\text{in}}(k)+Z_0}\right| \tag{13}$$

indicating that the coupling magnitude has a significant impact on matching depth.

On the other hand, inside the optimum region, the resonance frequency shows weak sensitivity to vertical spacing, which can be written as

$$\frac{\partial f_0}{\partial z_{\text{par}}} \approx 0 \tag{14}$$

As illustrated in Fig. 7, varying the gap spacing, for example, z_{par} from (−0.5 to −1.5) mm, only slightly affects the resonance, which remains centered at 31.5 GHz. It can thus be noted that the parasitic element mainly tunes the strength of the electromagnetic coupling between the antennas.

Table 2: Optimized geometric design parameters of the high-tilt multilayer antenna.

Parameter	Value	Description	Parameter	Value	Description
Wg	15.0	Ground plane width	*Wf*	0.6	Feed line width
Lg	15.0	Ground plane length	*Iset*	0.65	Inset depth
Hs	0.787	RT5880 thickness	*SL*	1.7	Slot length
T	0.035	Copper thickness	*SW*	0.25	Slot width
Ha1	0.9	Lower Rohacell gap	*SA*	18°	Slot angle
Ha2	0.6	Upper air gap	*Lp2*	2.9	Parasitic length
Lp	3.4	Radiator length	*Wp2p*	3.2	Parasitic width
Wp1	4.0	Upper width	*Dp2x*	0.25	X-offset
Wp2	2.8	Lower width	*Dp2y*	0.15	Y-offset
Dx	0.35	X-asymmetry	*Dy*	0.25	Y-asymmetry

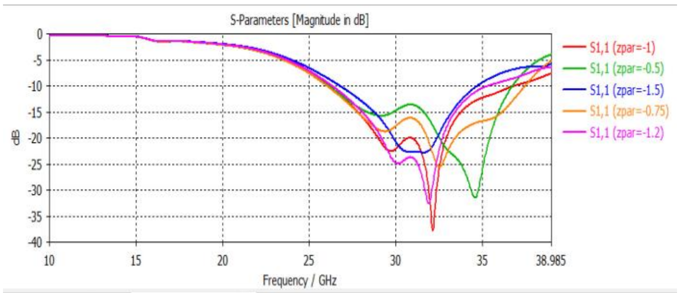

Fig 7. Simulated S_{11} For Different Parasitic Director Heights Zpar

In addition, the extent of impedance matching is highly sensitive to the gap spacing between the antennas. The best impedance matching occurs when $z_{par} = -1.0$ mm, as illustrated by the red curve, where the reflection coefficient is approximately −38 dB. In this case, the antennas are well coupled, and power can be transferred efficiently to the parasitic layer without causing resonance instability.

Table 2 contains all of the structural details for the suggested antenna, including the asymmetric kite-patch characteristics and the multilayer stack-up dimensions. The optimum results from the parametric analysis to reach the desired 49.0° beam squint at 31.5 GHz are represented by these numbers.

iii- Aperture Phase Evolution and Passive Beam-Steering Mechanism

The four design stages are shown in the simulated aperture phase distribution of fig 8. Based on the aperture antenna theory, the steering angle depends on the transverse aperture phase gradient,

$$\theta_0 = \sin^{-1}((\lambda_0/(2\pi))(d\varphi/dx)) \quad (15)$$

$d\varphi/dx$ is the aperture phase gradient. The beam tilt is thus obtained by formation of a non-uniform aperture phase distribution (APD) and not by active phase excitation. Case 1 is that of a conventional rectangular patch, which shows an almost symmetric aperture phase with little transverse phase variation and thus radiates in broadside. Case 2 adds the kite-shaped radiator and the diagonal slot, which makes the electrical current path longer and establishes the initial phase asymmetry. The phase gradients extracted from the Fig.8 reveal the kite-shaped reflow of the patch boundary, which is the most significant phase gradient change. In Case 3, the asymmetric 6:4 via fence changes the local surface-wave propagation constant, thus increasing the transverse phase imbalance and significantly increasing the aperture phase gradient. Finally, the mutual coupling of the parasitic director in Case 4 produces a smooth enough phase variation to produce an approximately linear phase variation across the aperture, which steers the main beam to an angle of approximately 49°.

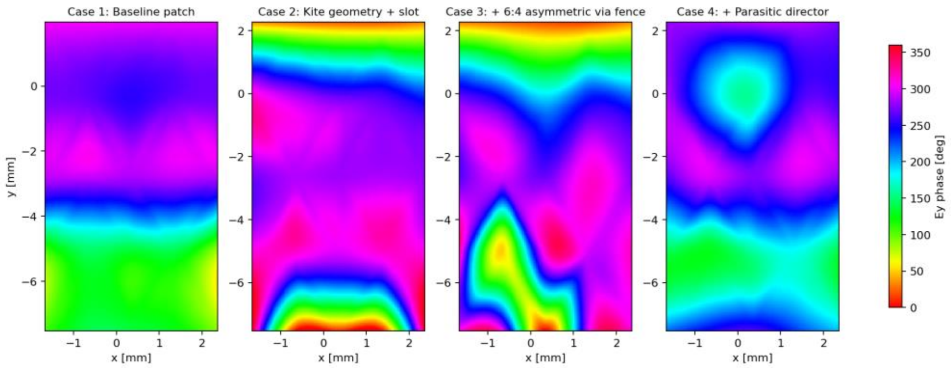

Fig. 8. Simulated Aperture Phase Distribution for the Four Design Stages

The simulated aperture phase maps are consistent with the theoretical aperture-field prediction, which is the sum of the phase contributions from the kite geometry, the diagonal slot and the asymmetric via fence, and the parasitic director.

V. Results and Discussion

Field And Current Distribution Analysis

i. H-Field Distribution

The simulated magnetic field (H-field) distribution at 31.5 GHz is shown in Fig. 9. The results indicate that the electromagnetic energy is strongly confined within the region enclosed by the non-uniform via-fence structure. A pronounced H-field concentration is observed around the diagonal reactive slot, which functions as the primary electromagnetic coupling interface between the feed line and the kite-shaped radiator. The rapid attenuation of the magnetic field outside the via-fence boundary provides clear evidence of an effective magnetic-wall behavior. This confinement technique effectively minimizes the propagation of the substrate-bound surface waves, reducing the energy leakage in the lateral direction. Hence, the back radiation and edge diffraction are reduced, which is helpful in obtaining a high Front-to-Back Ratio (FBR) of 23.7 dB with the radiation pattern remaining intact.

ii. Surface current distribution

The surface current distribution for 31.5 GHz in Fig. 10 differs in symmetry from that generally observed in standard microstrip patch antennas. In this antenna, asymmetry is incorporated in the design by introducing a diagonal reactive slot with a 15° angle and two different patch widths: $Wp_1 = 4.0$ mm and $Wp_2 = 2.8$ mm. These unequal paths of current flow are along the two sides of the radiator element of the antenna. The imbalance in the design of the antenna causes a particular phase difference in the radiating aperture. The primary radiation lobe tilts up to 49.0° in the E-plane due to the phase difference between the patch's opposing edges. The strong confinement of the magnetic field and the imbalance in the surface currents are the two main factors that cause the passive tilting of the antenna without the use of any active phase shifter networks.

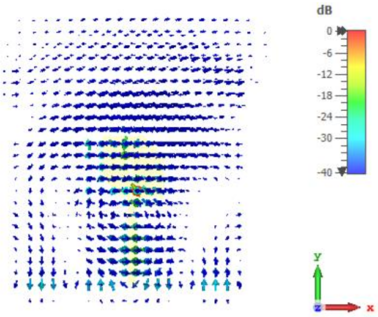

Fig. 9. H-Field Surface-Wave Suppression

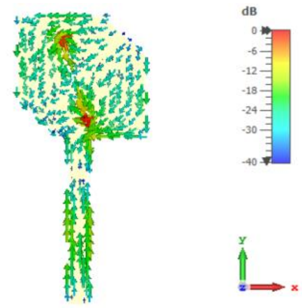

Fig. 10. Surface Current Distribution

iii. Antenna Performance After UAV Platform Integration

In order to validate the proposed antenna for practical deployment, the same antenna is simulated after being mounted on a representative UAV platform, as shown in Fig .11. Comparison of simulations with three different configurations is shown: (A) free space, (B) direct mounting (0 mm gap), and (C) a 5 mm air gap. The resonant frequency and the impedance matching S11 results are only slightly different, as shown in Fig. 12, indicating good stability of the impedance characteristics under practical mounting conditions.

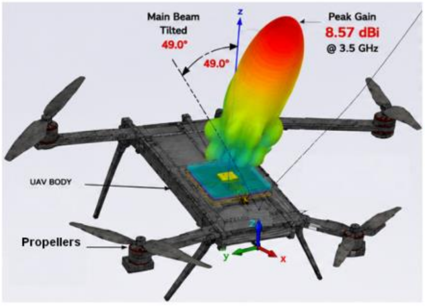

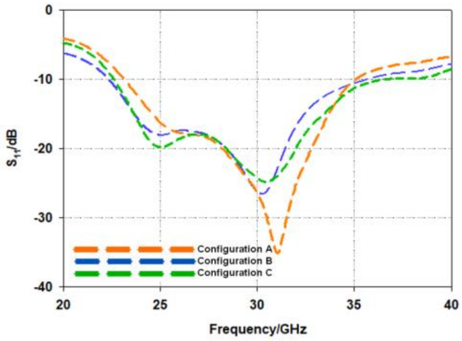

Fig.11. Antenna Integrated on UAV Platform. **Fig.12.** Comparison of simulated S_{11}

iv. Far-field radiation characteristics and high-tilt performance

The simulated normalized far-field radiation patterns in the principal E-plane (φ = 0°) and H-plane (φ = 90°) are presented in Fig. 13. The Far Field Radiation Characteristics and UAV Integration Performance are presented. The radiation pattern of the simulated antenna in both E-plane and H-plane is compared with the normalized radiation pattern as shown in Fig. Three configurations were tested with 9 and 10: that of the standalone antenna, the direct mounting of the antenna on the UAV, and the mounting of the antenna with a 5 mm air gap. The standalone antenna has a passive beam tilt of 49°, a realized gain of 8.24 dBi, a front-to-back ratio of 23.7 dB, and a sidelobe level of less than −18.6 dB. Direct mounting of the UAV will cause the beam tilt to be 63° and introduce noticeable pattern distortion due to electromagnetic coupling, which will affect the radiation characteristics. The presence of a 5 mm air gap allows the beam tilt to be restored to 48°, and the normalized E-plane and H-plane patterns are very close to the patterns of the standalone antenna. These results show that the proposed air-gap effectively suppresses platform-induced coupling while maintaining the required beam-steering performance for 5G/6G communications in UAV Applications.

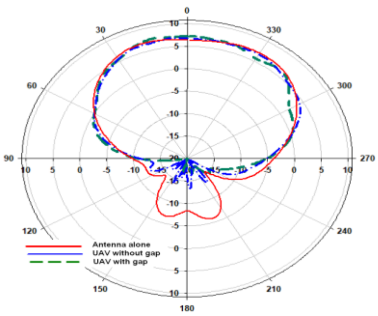

(a)

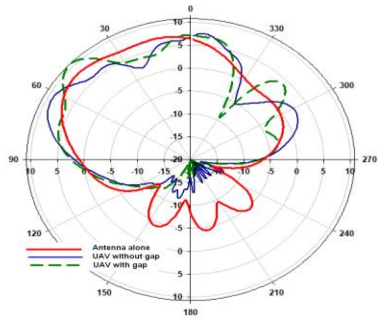

(b)

Fig. 13. Normalized radiation pattern comparison: (a) E-plane and (b) H-plane.

To assess how effectively interference is reduced, we normalized the entire 360° radiation pattern to the peak level. The level of side lobe remains below –18.6 dB; hence, secondary lobe reduction is significant. This level of reduction is critical in a 5G environment where secondary radiation may cause co-channel interference and compromise link quality.

The antenna also confirms significant backward radiation suppression with a front-to-back ratio (FBR) of 23.7 dB. This performance is made possible by the via-fence structure's shielding action and the ground-plane's optimized dimensions (15 x 15 mm²), which together lessen the development of backlobes and improve forward directivity. The proposed antenna also achieves a cross-polarization discrimination (XPD) of ~14.7 dB at 30 GHz, which is considered good polarization purity for mmWave UAV communications. Table .3 exhibits a comparison of the proposed antenna with some recent beam-tilted mmWave antennas with respect to operating frequency, antenna size, realized gain, beam tilt/scan angle, radiation efficiency, total efficiency, aperture efficiency, and structural complexity.

Table 3: Comparison of the proposed antenna with state-of-the-art beam-tilted

Ref.	Structural Complexity	Freq. Range (GHz)	Size (mm²)	Realized Gain (dBi)	Beam Tilt/Scan (°)	Rad. Eff. (%)	Total Eff. (%)	Aperture Eff. (%)
[V]	High (SIW array)	25.43–26.91	232.6×257	30.71–32.80	Broadside	>52	N/R	N/R
[XXX] LP-CB	Medium (planar bent-CSIW, LP, no vias)	24.2–30	~30.5×30.5	9.2	24 ± 1 (passive)	N/R	>86	N/R
[XXX] CP-CB	Medium (planar bent-CSIW + slotted ground, CP, no vias)	26.8–31.2	~30.5×30.5	7.5	24 ± 1 (passive)	N/R	>80	N/R
[XXII]	Low (monopole + elliptical slot)	25.83–30.24	5×3	~4	Broadside	89	N/R	N/R
[XXVI]	Very High (1×8 array)	24–30	12×60	≥11.8	±75	>75	N/R	N/R
This work	**Medium (two-layer single-element)**	**25–32**	**15×15**	**8.58**	**49 (passive)**	**87.1**	**86.1**	**≈81.7**

Overall, the findings show that without adding structural complexity, the suggested architecture gives high beam tilt, steady orthogonal-plane performance, and superior suppression characteristics.

V. Conclusion

A novel high-tilt microstrip antenna for 30 GHz operation has been proposed. The radiator is kite-shaped, and the non-uniform capacitive via fence is in a 6:4 ratio. The tilt angle is 49° without the need for active phase shifters and complex multilayer constructions. The surface current and H-field analysis show the effectiveness of structural asymmetry in creating a synthetic phase gradient, thus allowing for off-axis radiation with very low back-lobe radiation. The design has a peak realized gain of 8.3 dBi with clean and high-quality radiation patterns. In comparison with previous works, the design provides a simple and cost-effective solution for mm-Wave 5G applications. The analysis shows the effectiveness of the antenna in high-performance wireless applications with the need for broad off-axis coverage.

Conflict of Interest :

The authors declare that there is no conflict of interest regarding this paper.

References

I. Akdeniz, Mustafa R., et al. "Millimeter Wave Channel Modeling and Cellular Capacity Evaluation." IEEE Journal on Selected Areas in Communications, vol. 32, no. 6, 2014, pp. 1164–1179. 10.1109/JSAC.2014.2328154

II. Alreshaid, S. A., M. S. Sharawi, S. S. Podilchak, and M. M. Tentzeris. "Millimeter-Wave-Printed Antenna Arrays for 5G Applications." Handbook of Antenna Technologies, edited by Z. N. Chen, Springer, 2016, pp. 2743–2789. 10.1007/978-981-4560-44-3135

III. Amin, M., R. Cahill, and V. Fusco. "Single Feed Low Profile Omnidirectional Antenna with Slant 45° Linear Polarization." IEEE Transactions on Antennas and Propagation, vol. 55, no. 11, 2007, pp. 3087–3090. 10.1109/TAP.2007.908826

IV. Anim, K., J.-N. Lee, and Y.-B. Jung. "High-Gain Millimeter-Wave Patch Array Antenna for Unmanned Aerial Vehicle Application." Sensors, vol. 21, no. 11, 2021, p. 3914. 10.3390/s21113914

V. Anim, K., J.-N. Lee, and Y.-B. Jung. "Multi-Band Unmanned Aerial Vehicle Antenna for Integrated 5G and GNSS Connectivity." Telecom, vol. 6, no. 2, 2025, pp. 38–52. 10.3390/telecom6020038

VI. Bahl, I. J., and P. Bhartia. Microstrip Antennas. Artech House, 1980.

VII. Balanis, Constantine A. Antenna Theory: Analysis and Design. 4th ed., Wiley, 2016.

VIII. Beaskoetxea, U., et al. "3-D-Printed 96 GHz Bull's-Eye Antenna with Off-Axis Beaming." IEEE Transactions on Antennas and Propagation, vol. 65, no. 1, 2017, pp. 17–25. 10.1109/TAP.2016.2628322.

IX. Borhani Kakhki, M., et al. "Millimeter-Wave Beam-Tilting Vivaldi Antenna with Gain Enhancement Using Multilayer FSS." IEEE Antennas and Wireless Propagation Letters, vol. 17, no. 12, 2018, pp. 2279–2283. 10.1109/LAWP.2018.2873113

X. Chacko, B. P., G. Augustin, and T. A. Denidni. "Tilted-Beam MPA with Broad-Useful Bandwidth." IET Microwaves, Antennas & Propagation, vol. 11, no. 4, 2017, pp. 487–492. 10.1049/IET-MAP.2016.0237

XI. Chakravarty, S., et al. "A Metasurface-Enabled Lens Antenna Demonstrating Electromechanical Beam-Tilting for 5G Applications." Proceedings of the National Conference on Communications (NCC), 2022, pp. 277–281. 10.1109/NCC55593.2022.9806743

XII. Chen, S., et al. "Wideband and High Gain Array Antenna for 5G Smart Phone Applications Using Frequency Selective Surface." IEEE Access, vol. 10, 2022, pp. 73157–73165. 10.1109/ACCESS.2022.3196687

XIII. Chen, Z. N., et al., editors. Handbook of Antenna Technologies. Springer, 2016. 10.1007/978-981-4560-44-3

XIV. Costa, F., A. Monorchio, and G. Manara. "Analysis and Design of Ultra-Thin Electromagnetic Absorbers Comprising Resistive FSS." IEEE Transactions on Antennas and Propagation, vol. 58, no. 5, 2010, pp. 1551–1558. 10.1109/TAP.2010.2044356

XV. Dadgarpour, A., et al. "Mutual Coupling Reduction in Dielectric Resonator Antennas Using Metasurface Shield for 60-GHz MIMO Systems." IEEE Antennas and Wireless Propagation Letters, vol. 16, 2017, pp. 477–480. 10.1109/LAWP.2016.2585127

XVI. Ellis, M. S., et al. "Compact Wideband Printed Antenna with Circularly Polarized Tilted Beam Radiation Using a Quasi-Radiator." AEU – International Journal of Electronics and Communications, vol. 170, 2023, p. 154883. 10.1016/j.aeue.2023.154883

XVII. Fadhil, T. Z., et al. "Broadside Gain Enhancement of Wideband Monopole Circular Shaped Antenna Using FSS for Sub-6 GHz Applications." Infocommunications Journal, vol. 16, no. 3, 2024, pp. 82–88. 10.36244/ICJ.2024.3.8

XVIII. Gharaati, A., et al. "A Novel Single-Layer Microstrip Antenna with Tilted Radiation Pattern." Proceedings of the International Symposium on Antennas and Propagation (ISAP), 2021, pp. 479–480. 10.1109/IEEECONF35879.2020.9330222

XIX. Hong, W., et al. "Study and Prototyping of Practically Large-Scale mmWave Antenna Systems for 5G Cellular Devices." IEEE Communications Magazine, vol. 52, no. 9, 2014, pp. 63–69. 10.1109/MCOM.2014.6894454

XX. Hong, W., K. Baek, and S. Ko. "Millimeter-Wave 5G Antennas for Smartphones: Overview and Experimental Demonstration." IEEE Transactions on Antennas and Propagation, vol. 65, no. 12, 2017, pp. 6250–6261. 10.1109/TAP.2017.2735459

XXI. Hur, S., et al. "Millimeter Wave Beamforming for Wireless Backhaul and Access in Small Cell Networks." IEEE Transactions on Communications, vol. 61, no. 10, 2013, pp. 4391–4403. 10.1109/TCOMM.2013.090513.120848

XXII. Kumar, P., T. Ali, O. P. Kumar, S. Vincent, P. Kumar, Y. Nanjappa, and S. Pathan. "An Ultra-Compact 28 GHz Arc-Shaped Millimeter-Wave Antenna for 5G Application." Micromachines, vol. 14, no. 1, 2023, p. 5. 10.3390/mi14010005

XXIII. Li, M., et al. "A Compact, Single-Layer, Index-Modulated Microstrip Antenna with Stable Customized Tilted Beam over a Wide Bandwidth." IEEE Transactions on Antennas and Propagation, vol. 70, no. 12, 2022, pp. 11428–11441. 10.1109/TAP.2022.3213997

XXIV. Li, M., et al. "Low-Profile and Wide-Beamwidth Dual-Polarized Distributed Microstrip Antenna." IEEE Access, vol. 8, 2020, pp. 155085–155092. 10.1109/ACCESS.2020.3018501

XXV. Li, Y., et al. "Axial Ratio Bandwidth Enhancement of 60-GHz Substrate Integrated Waveguide-Fed Circularly Polarized LTCC Antenna Array." IEEE Transactions on Antennas and Propagation, vol. 60, no. 10, 2012, pp. 4619–4626. 10.1109/TAP.2012.2207323

XXVI. Lin, J., Y. F. Cao, W. Che, and W. Xue. "Wide-Angle and Wideband Millimeter-Wave Beam-Scanning Array Using Multimode Shorted Patch Antenna Elements for Unmanned Aerial Vehicle Communication." IEEE Transactions on Vehicular Technology, vol. 73, no. 11, 2024, pp. 16285–16298. 10.1109/TVT.2024.3462456

XXVII. Liu, D., X. Zhang, and Y. Zhang. "A Compact Dual-Polarized Antenna for 5G MIMO Applications." IEEE Transactions on Antennas and Propagation, vol. 67, no. 6, 2019, pp. 4000–4005. 10.1109/TAP.2019.2905777

XXVIII. Liu, Z., Y. He, and Y. Li. "Beamwidth Enhancement of Microstrip Antennas Using Capacitive Via-Fence Loading." IEEE Open Journal of Antennas and Propagation, vol. 4, 2023, pp. 136–145. 10.1109/OJAP.2023.3239817

XXIX. Ojaroudiparchin, N., et al. "A Switchable 3-D-Coverage-Phased Array Antenna Package for 5G Mobile Terminals." IEEE Antennas and Wireless Propagation Letters, vol. 15, 2016, pp. 1747–1750. 10.1109/LAWP.2016.2532607

XXX. Patel, A., W. G. Whittow, and C. J. Panagamuwa. "Millimeter-Wave Conical Beam Antennas for Drone and Vehicle Communications." IEEE Access, vol. 13, 2025, pp. 172496–172506. DOI: 10.1109/ACCESS.2025.3617174

XXXI. Rappaport, Theodore S., et al. "Wireless Communications and Applications above 100 GHz: Opportunities and Challenges for 6G and Beyond." IEEE Access, vol. 7, 2019, pp. 78729–78757. 10.1109/ACCESS.2019.2921522

XXXII. Sharawi, M. S. "Printed Multi-Band MIMO Antenna Systems and Their Performance Metrics." IEEE Antennas and Propagation Magazine, vol. 55, no. 5, 2013, pp. 218–232. 10.1109/MAP.2013.6735522

XXXIII. Shi, J., et al. "A Microstrip Yagi with an Enlarged Beam Tilt Angle." IEEE Antennas and Wireless Propagation Letters, vol. 18, no. 5, 2019, pp. 999–1003. 10.1109/LAWP.2019.2901033

XXXIV. Shi, J., et al. "An Omnidirectional Circularly Polarized Antenna Array." IEEE Transactions on Antennas and Propagation, vol. 64, no. 2, 2016, pp. 574–581. 10.1109/TAP.2015.2509012

XXXV. Tamara Z., NOOR A. MURAD, et al. "Design and Performance of a Compact Circular Patch Antenna with Metasurface Superstrate for Fifth Generation Application." 2023 IEEE 16th Malaysia International Conference on Communication (MICC), IEEE, 2023. 10.1109/MICC59384.2023.10419571

XXXVI. Tong, X., et al. "Low-Profile, Broadband, Dual-Linearly Polarized, and Wide-Angle Millimeter-Wave Antenna Arrays for Ka-Band 5G Applications." IEEE Antennas and Wireless Propagation Letters, vol. 20, no. 11, 2021, pp. 2038–2042. 10.1109/LAWP.2021.3102375

XXXVII. Yao, Y., et al. "Wideband Circularly Polarized Antipodal Curvedly Tapered Slot Antenna Array for 5G Applications." IEEE Journal on Selected Areas in Communications, vol. 35, no. 7, 2017, pp. 1539–1549. 10.1109/JSAC.2017.2699098

XXXVIII. Zhang, J., et al. "A Bending-Insensitive Ku-Band SIW Microstrip Antenna with Tilted Beam Capability." Journal of Electromagnetic Waves and Applications, vol. 39, no. 3, 2024, pp. 412–427. 10.1080/09205071.2024.2430618